Laser Doppler Velocimeter Measurements in Unsteady, Separated, Transonic Diffuser Flows

J. T. Salmon,* T. J. Bogar,† and M. Sajben‡
McDonnell Douglas Corporation, St. Louis, Missouri

A laser Doppler velocimeter was used to measure the streamwise velocity component in unsteady separated flowfields in a two-dimensional transonic diffuser with and without externally induced periodic fluctuations. Results are also presented for fully attached, unsteady, unexcited flow. The time-dependent perturbation flowfield associated with the external excitation was determined throughout the subsonic region for a case with shock-induced separation. The results indicate that a transverse, wavelike motion of the boundary-layer/core-flow interface is an important aspect of the overall oscillations and overwhelms effects associated with acoustic-wave propagation.

Nomenclature

A = amplitude coefficient in Fourier series
f = excitation frequency
h = channel height
M = Mach number
N = number of velocity samples
T = temperature
$\bar{u}$ = mean streamwise velocity
$\hat{u}$ = rms of streamwise fluctuating velocity component
$\underline{u}$ = ensemble-averaged streamwise velocity
$\tilde{u}$ = periodic component of ensemble-averaged streamwise velocity
$\tilde{x}$ = dimensionless streamwise coordinate; x/h_*, $\tilde{x}=0$ at throat
$\tilde{y}$ = dimensionless vertical coordinate; y/h_*, $\tilde{y}=0$ at lower wall
α = perturbation phase angle
$\tilde{\delta}^*$ = dimensionless displacement thickness, δ^*/h_*
ϕ = phase angle in Fourier series
$\tilde{\theta}$ = dimensionless momentum thickness, θ/h_*

Subscripts

e = exit
ℓ = lower wall
m = midstream ($\tilde{y}=0.432$)
n = Fourier harmonic
o = plenum
r = reference
s = static
t = total
u = upper wall
σ = shock
$*$ = throat

Introduction

THIS paper contains one of three related descriptions of recent experimental studies of unsteady, transonic flows in a two-dimensional diffuser.[1,2] The flows exhibit features similar to those in supersonic inlets of air-breathing propulsion systems of aircraft and missiles. Naturally occurring, self-sustaining oscillations, generically equivalent to dynamically distorted flowfields found in operational inlets, were found under all operating conditions. Externally forced oscillations occurring in response to perturbations imposed at the downstream end were also studied. These oscillations simulate pressure oscillations that occur in ramjet inlets in response to combustor instabilities.[3] Also, the deterministic nature of the forced oscillations qualifies them as appropriate test cases for advanced computational methods for time-dependent flows. The unsteady aspects of these flows are of interest because inlet performance is generally limited by the appearance of undesirable low-frequency fluctuations and a credible prediction of off-design performance must therefore explicitly include such unsteady effects.

The three papers derive from a long-term program designed to contribute to the scientific observational base necessary for the proposed prediction capability. The program has so far dealt with exploring and characterizing flows in nominally two-dimensional, supercritically operated diffusers, with special emphasis on unsteady behavior. Several configurations have been investigated and reported, with exit-to-throat area ratios ranging from 1.84 to 2.37.[4-7] In the previous models, the basic flow pattern consistently was found to be one of the two basic types shown in Fig. 1, regardless of area ratio. Below a shock Mach number of approximately 1.3, the flow displayed a pressure-gradient-induced separation, while at higher shock strengths, the separation was induced by the shock. The two types of flows are drastically different in terms of most measured steady and unsteady properties. Naturally present, self-sustaining oscillations were found in all models at all flow conditions.

This paper and Refs. 1 and 2 provide a detailed description of experiments with a 1.52 area-ratio diffuser and a correspondingly mild streamwise rate of area change (Fig. 2). Unlike previous models, the flow was fully attached everywhere up to a shock Mach number of 1.27. Beyond this Mach number, shock-induced separation occurred, as was the case with earlier models. Self-sustaining oscillations were also present at all conditions, but at markedly lower amplitudes than previously encountered.[7] Provisions were made to mechanically modulate the exit area of this model and thereby force the entire diffuser flow into periodic oscillation at frequencies up to 330 Hz.

The experimental apparatus, the instrumentation, and measurements of the time-mean flowfield are reported in Ref. 1, along with a study of naturally occurring unsteadiness. Dynamic pressure and shock position measurements with

Presented as Paper 81-1197 at the AIAA 14th Fluid and Plasma Dynamics Conference, Palo Alto, Calif., June 23-25, 1981; submitted July 13, 1981; revision received June 4, 1982.

*Senior Engineer, McDonnell Douglas Research Laboratories; currently Graduate Student, Dept. of Mechanical Engineering, Purdue University, W. Lafayette, Ind.

†Scientist, McDonnell Douglas Research Laboratories. Senior Member AIAA.

‡Principal Scientist, McDonnell Douglas Research Laboratories. Associate Fellow AIAA.

forced oscillations are reported in Ref. 2. The present paper is focused on laser Doppler velocimeter measurements, made with fine spatial and temporal resolution, for three selected cases with natural and forced oscillations.

Experimental Apparatus

This section briefly describes the model and the laser Doppler velocimeter (LDV) system used. A detailed description of the diffuser model, the test facility, and the nonlaser diagnostic techniques employed are given in Ref. 1.

The exit-to-throat area ratio of the diffuser model (Fig. 2) is 1.52, and the width-to-height ratio of the minimum-area (throat) cross section is 4.03. The throat height of 44. 1 mm is used to normalize all length dimensions throughout this paper. The distance from the throat to the end of the divergent, contoured portion of the top wall is 7.2 throat heights. The channel continues with a constant-area segment, which is also 7.2 throat heights long. Sidewalls are made of 25.4-mm-thick, schlieren-quality glass, flat to within an optical wavelength over a length of 25 cm. Dielectric coatings on all optical surfaces provide minimum reflectivity at 500 nm.

Periodic modulation of the exit cross-sectional area is accomplished by a triangular, full-span rotor located at $\tilde{x}=12.97$; the rotor is driven by a variable-speed motor at shaft frequencies up to 110 Hz, corresponding to excitation frequencies up to 330 Hz. The speed of rotation was kept constant within 1%. The radius to the rotor tips is 25.4 mm, and the maximum height of the vertices above the bottom wall is 6.3 mm. A digital encoder, mounted rigidly on the rotor shaft, provides a pulse train of 360 pulses per rotor revolution; this signal is used to synchronize the data with the instantaneous position of the rotor.

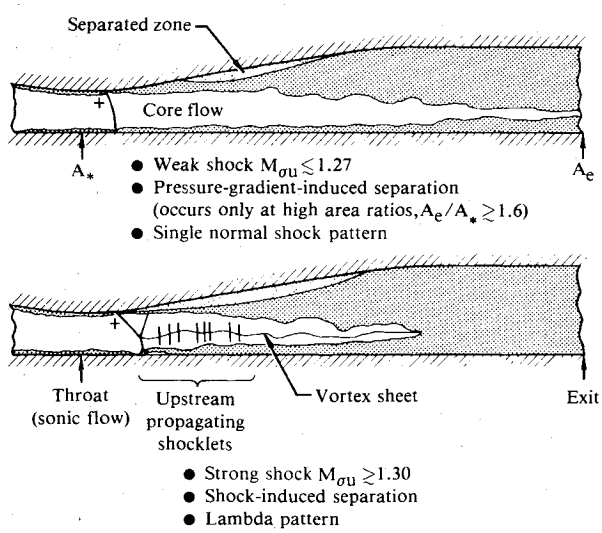

Fig. 1 Flow patterns observed in supercritical diffuser flows. $M_{\sigma u}$ is local Mach number at plus sign.

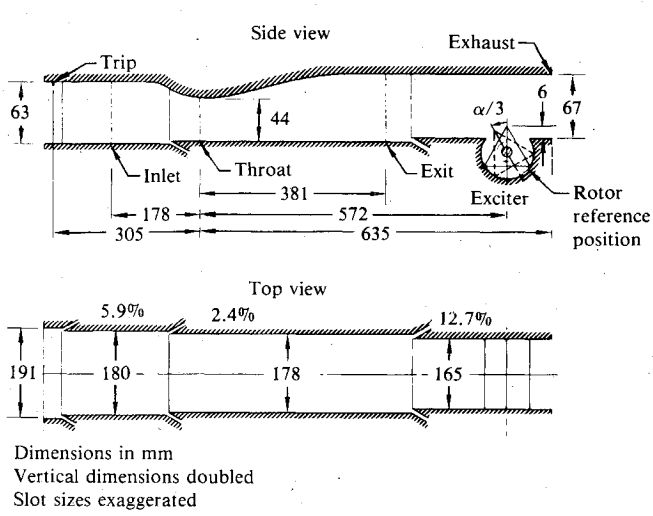

Fig. 2 Schematic of transonic diffuser model.

Measurements of the horizontal velocity component, u, were made using a single-channel LDV, aligned in a dual-beam, off-axis, forward-scatter configuration (Fig. 3). The light source was a 4-W argon-ion laser operated at 514.5 nm. The probe volume was formed by splitting the beam and focusing it approximately 600 mm from the focusing lens, with each beam converging 1.007 deg to the optical axis. The optical axis was aligned normal to the diffuser sidewalls. This optical arrangement produced a probe volume with a streamwise resolution of 0.46 mm and a fringe spacing of 14 μm. The receiving optics were set at 20 deg from the optical axis to provide an effective spanwise resolution of the probe volume of 3.6 mm. Reverse flow was measured by incorporating a Bragg cell in the optical path between the beamsplitter and the transmitting lens to shift the center frequency from dc to 40 MHz.

Scattered light from particles traversing the probe volume was converted by a photomultiplier tube to an analog signal which was processed by a counter-type LDV processor. The counter employed adjustable threshold and overload-reset settings in conjunction with a Schmitt trigger for digitizing the analog signal and a 10:16 comparator logic circuit which ensured the processing of only Doppler bursts. The digital output from the processor was fed into one channel of a two-channel buffer. In forced oscillation runs, a second buffer channel was used to record simultaneously the angular position of the rotor from the digital encoder. When the buffers were full, data from both channels were automatically transferred to digital tape for future processing.

The entire optical table was mounted on an x-y-z traversing unit which was controlled by manually operated stepper motors. The position along each axis was determined by precision sliding potentiometers mounted in bridge circuits connected to digital voltmeters. The absolute positions, accurate to within 0.4 mm, were digitized and stored on tape along with the velocity data. The relative positions between spatial points were accurate to within 0.08 mm.

The air supplied to this facility was dry and filtered, requiring supplementary seeding in the plenum chamber by a variable (one to six jets) atomizer. The atomizer specifications stated a mean droplet geometric diameter of 0.8 μm and a geometric standard deviation <2.0 for dioctyl phthalate. The oil was diluted with ethanol to 50 vol.% to reduce droplet sizes further by alcohol evaporation during transit from the atomizer to the probe volume.

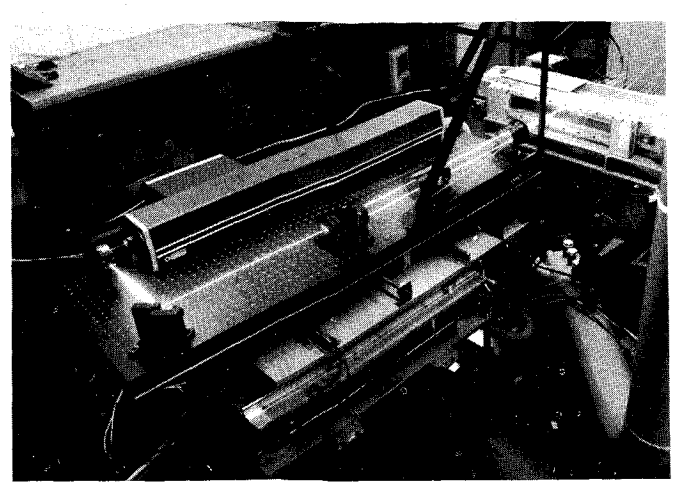

Fig. 3 Laser velocimeter system in operation with diffuser model.

Flow Conditions

Flow conditions were characterized by the local Mach number immediately before the shock, just outside of the upper-wall boundary layer (M_{ou}). This Mach number controls the pressure increase imposed on the top-wall boundary layer across the shock and thereby largely determines the character of the shock/boundary-layer interaction.

LDV measurements were made at two typical flow conditions: $M_{ou}=1.235$, corresponding to attached flow on both walls, and $M_{ou}=1.353$, displaying shock-induced separation on the upper wall and no observable separation on the bottom wall. These two conditions will be referred to as the weak and strong shock cases, respectively. Both cases have been explored in detail in Ref. 1 where a thorough discussion of the major features of this flow is presented. Characteristic flow properties are listed in Table 1. In particular, there are two distinct spectral peaks in the shock-displacement spectra in the weak shock case (at $f_1=60$ Hz and at $f_2=230$ Hz) and only one in the case of the strong shock (at $f_1=217$ Hz).

The weak shock case was explored only without excitation, whereas the strong shock case was mapped both with and without excitation. In the latter case, the excitation frequency was 300 Hz—38% above the natural frequency—to avoid any singular behavior that might be associated with a possible resonance.

The mechanical area modulation produced pressure fluctuations throughout the system. At the exit location ($\bar{x}=8.65$) these fluctuations were monitored by four high-response pressure transducers flush mounted in pairs on the top and bottom walls. Examination of the signal showed them to be dominated by the fundamental (excitation) frequency.

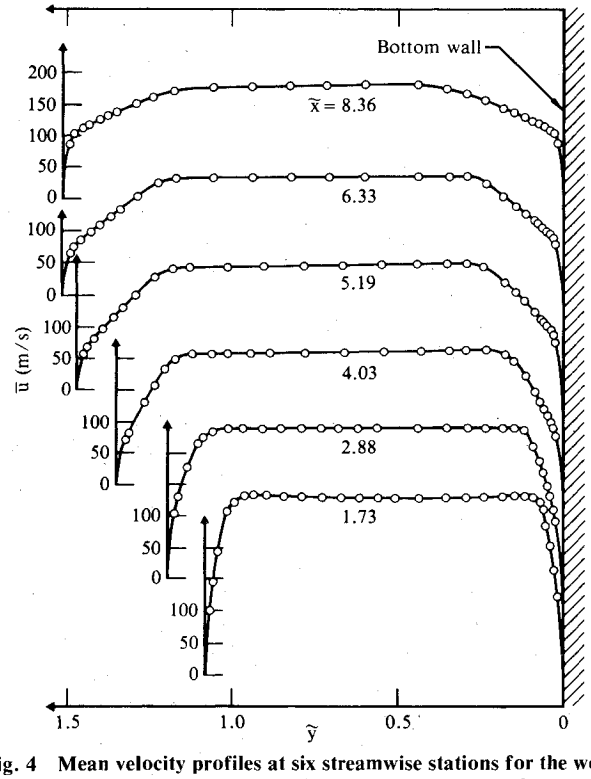

Fig. 4 Mean velocity profiles at six streamwise stations for the weak shock case ($M_{ou}=1.235$). Left vertical axes are located at the top wall for a given $\bar{x}$.

Furthermore, the four signals had nearly identical magnitude and phase, indicating a nearly planar pressure wave, despite the asymmetry of the excitation technique. The rms value of the first harmonic was 0.57% of the local time-mean static pressure, i.e., the forcing represented a small-amplitude perturbation of the flow.

The exit pressure fluctuations in this experiment can be considered as the simulated equivalents of ramjet burner pressure oscillations. Also, in a theoretical analysis, they represent a time-dependent exit boundary condition driving the flow and would be used as inputs in computations intended to verify a theoretical approach. The degree of two-dimensionality of the flows studied here is discussed in Ref. 1.

Data Acquisition and Reduction

The spatial resolution chosen for the velocity survey was sufficient to determine boundary-layer profiles and the interior structure of the separated zone. For the strong shock case, velocity data were taken at 29 vertical positions for each of 11 streamwise locations, providing a matrix of 319 spatial points. The vertical spacing was smallest near the walls and largest in the core flow. For the weak shock case, the shock was further upstream, and two additional vertical profiles were inserted for a total of 377 points. All data were taken in the plane of symmetry of the model.

The velocity sampling rate ranged from approximately 500 Hz near the walls to greater than 1.5 kHz in the core flow. These data rates were insufficient for a direct temporal resolution of either the natural or the forced velocity field. However, information is still obtained concerning the fluctuating velocity field, using methods that depend on whether the flow is excited.

Data reduction was conventional for unexcited flows. The time-mean velocity was obtained by simple averaging, and the mean-square deviation of the fluctuating component was obtained by averaging the square of the variance.

For flows with forced oscillations, the periodic contributions to the velocity field were determined by an ensemble-averaging technique, utilizing the 360 pulse/rev pulse-train from the encoder in conjunction with a counter. The counter, whose output gave the angular rotor displacement, was automatically reset to zero at the reference rotor position [defined as the instant of maximum blockage, i.e., when an arbitrarily selected rotor vertex was located directly above the rotor axis (Fig. 2)]. The sense of the rotation was such that the vertex in the flow always moved upstream. At the instant of acquiring a velocity sample, the latest encoder count also was read, and the data were recorded as an ordered pair.

Since the rotor was triangular, the flow underwent three perturbation cycles for every rotor revolution. Each perturbation cycle was divided into 60 equal increments (denoted by subscript j), and the velocities, which had been recorded simultaneously with the encoder pulses, were sorted according to their associated perturbation phase angle α ($=j\times 6$ deg). (For practical reasons only 60 increments were used, even though 120 encoder pulses were available for each perturbation cycle.) The number of velocity samples N_j acquired in each perturbation phase interval varied from 2000 to 2500, providing an adequate measure of the fluctuation intensity. The mean velocity in each increment was calculated to form an ensemble-averaged waveform, $\tilde{u}(\alpha)$, of the streamwise velocity. This averaging eliminated fluctuations that were uncorrelated with the imposed excitation; therefore, the result

Table 1 Flow conditions

Shock strength	M_{ou}	p_{se}/p_{to}	M_e	$\bar{x}_{ou}$	$\bar{x}_{om}$	$\bar{x}_{am}$	f_1, Hz	f_2, Hz
Weak	1.235	0.826	0.51	1.41	1.47	0.014	60	230
Strong	1.353	0.722	0.62	1.98	2.39	0.063	217	—

describes the perturbation field with only minor harmonic contributions from the random field.

Fourier decomposition of the ensemble-averaged waveform yields

$$\underset{\sim}{u}(\alpha) = \bar{u} + u(\alpha) = \bar{u} + \sum_{n=1}^{\infty} A_n \cos(n\alpha - \phi_n) \qquad (1)$$

where u is the ensemble-averaged velocity, $\bar{u}$ is the time-mean velocity, and u is the periodic component. A_n and ϕ_n are the amplitude and phase of the nth Fourier component. Termination of the series at $n=5$ provided a sufficiently accurate representation of the waveform.

The rms velocity in each perturbation phase increment is

$$\hat{u}_j^2 = \frac{1}{N_j - 1} \sum_{i=1}^{N_j} (u_{ij} - u_j)^2 \qquad (2)$$

which provides a measure of the intensity of the random fluctuations. The total random contribution to the fluctuations can be determined by averaging over the cycle

$$\hat{u}^2 = \frac{1}{60} \sum_{j=1}^{60} \hat{u}_j^2 \qquad (3)$$

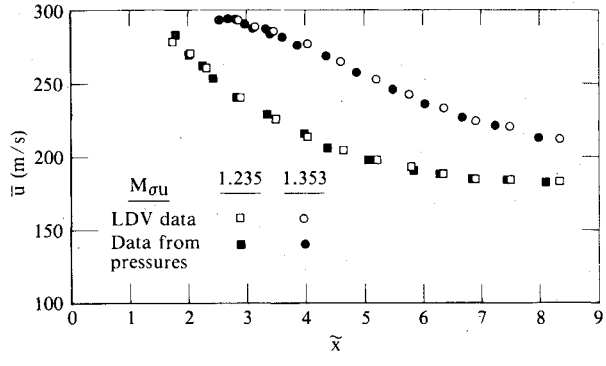

Fig. 5 Mean streamwise velocities measured with laser Doppler velocimeter and velocities determined from total/static pressure measurements, $\tilde{y}=0.432$.

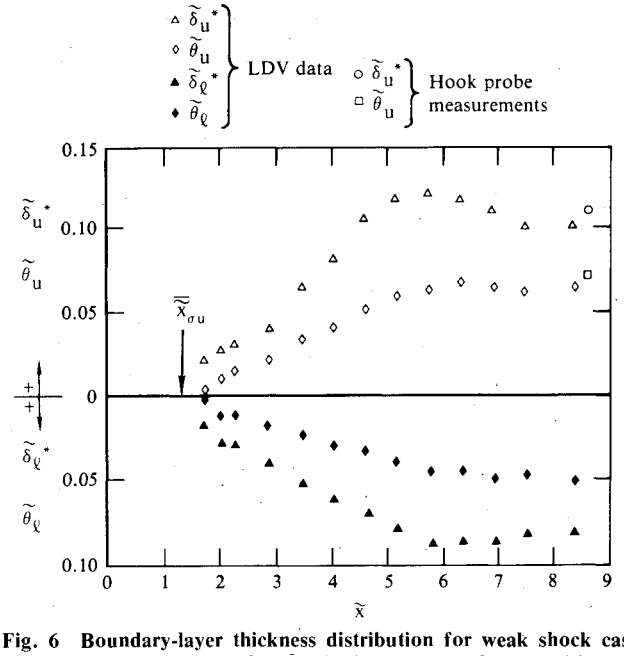

Fig. 6 Boundary-layer thickness distribution for weak shock case ($M_{\sigma u}=1.235$). Arrow labeled $\tilde{x}_{\sigma u}$ indicates mean shock positionon top wall.

During each run flow conditions were controlled by maintaining constant pressure ratios, and therefore Mach numbers. Temperature variations between surveys caused corresponding velocity variations, which were taken into account by multiplying the measured velocities by $(T_{ro}/T_{to})^{1/2}$, where the reference plenum temperature T_{ro} was set equal to 298 K. For this condition the sonic velocity at the throat is 316 m/s.

Discussion of Results

Weak Shock—No Excitation

Mean velocity profiles of the unperturbed flow are shown in Fig. 4. A clearly defined, inviscid core flow region exists at all stations. The streamwise velocity variation is illustrated in Fig. 5 (bottom curve). The core flow velocities were also determined from wall pressure data, plenum total temperature, and the local total pressure calculated from the plenum pressure and the normal shock relations. Velocities calculated in this manner, also shown in Fig. 5, agree well with the LDV measurements.

The existence of a well-defined core flow, and thereby a well-defined freestream velocity at the boundary-layer edge, permits unambiguous determination of characteristic boundary-layer thicknesses, as shown in Fig. 6. The local density was calculated using the measured local velocity and assuming the stagnation temperature to be constant throughout the boundary layer. Figure 6 also shows the respective thicknesses at the throat and at the exit stations.[1]

The results show that the top- and bottom-wall boundary layers are attached at all locations and of nearly equal thickness, although the top-wall layer increases in thickness slightly faster, being exposed to a slightly greater pressure gradient associated with the longitudinal curvature of the top wall. The data of Fig. 6 indicate no unexpected features and are well described by relatively simple theoretical models.[8]

The velocity information of Fig. 4, along with data from measured profiles located between them, was reduced further into contour plots of the mean streamwise velocity component as shown in Fig. 7a. (All such plots have the vertical scale doubled.) This figure clearly illustrates two attached boundary layers of nearly equal thickness. Small velocity overshoots occur at the edge of each boundary layer near the shock and also are observable in the original velocity profiles of Fig. 4. The origin of these overshoots is not clear; they may be due to the increasing obliqueness of the shock near the walls, resulting in correspondingly higher postshock velocities.

The spatial distribution of the fluctuating velocity component (Fig. 7b), which shows peaks in the upper and lower

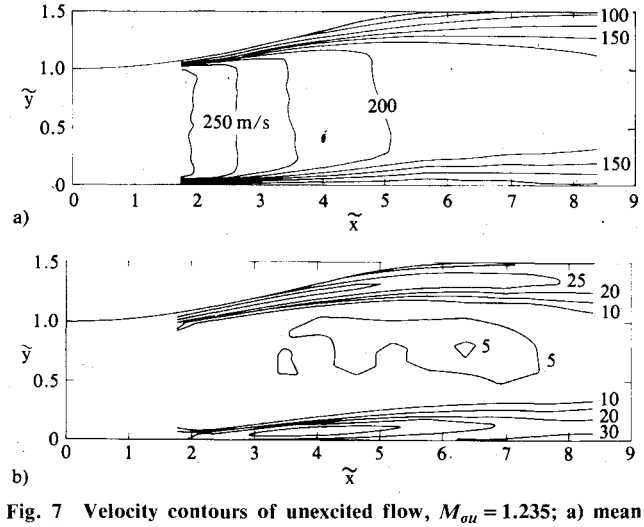

Fig. 7 Velocity contours of unexcited flow, $M_{\sigma u}=1.235$; a) mean velocity $\bar{u}$, b) fluctuating velocity $\hat{u}$.

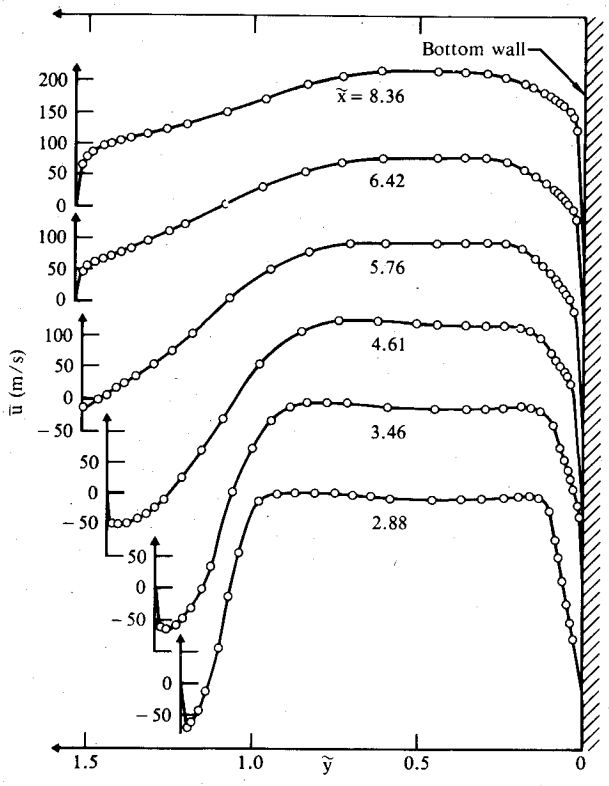

Fig. 8 Mean velocity profiles at six streamwise stations for the strong shock case ($M_{\sigma u} = 1.353$). Left vertical axes are located at the top wall for a given $\tilde{x}$.

shear layers and minimum values in the core flow, is consistent with the mean velocity distributions. Turbulence intensities ($\hat{u}/\bar{u}$) ranged from 2 to 3% in the core flow.

Strong Shock—No Excitation

The velocity profiles taken in this case clearly indicate a reversed flow region on the top wall and none on the bottom wall (Fig. 8). A well-defined core flow velocity no longer exists; it is distorted by significant velocity overshoots near the boundary-layer edges for $\tilde{x} \leq 6$ and beyond $\tilde{x} = 6$ byapparent merging of the two layers, making the concept of boundary layers marginally applicable to the flowfield. The velocity midway between the overshoot peaks was used as a nominal core flow velocity, whose distribution is given in Fig. 5. Again, the LDV data agree well with velocities computed from wall pressures. The core flow speeds in the strong shock case are considerably higher than those found with a weak shock, contrary to expectations based on one-dimensional, inviscid calculations. The reason for the opposite trend lies in the rapid growth of the top-wall boundary layer, illustrated by the boundary-layer thickness distributions of Fig. 9. The displacement thickness reaches a maximum shortly before the reattachment point at about 40% of the throat height or approximately 67 times the displacement thickness at the throat. The rapid growth interacts with the core flow and modifies the pressure distributions on both walls to reduce the pressure gradients as compared to the weak shock case. The reduced gradient reduces the growth of the attached bottom-wall boundary layer, which now is only about half as thick as in the weak shock case. The flow is grossly asymmetric and entirely dominated by the top-wall boundary layer.

The contour plot of Fig. 10a illustrates the mean flow features in two dimensions. In particular, the structure of the separated region is clearly visible. The separation bubble, as defined by the $\bar{u} = 0$ line, extends from the shock ($\tilde{x}_{\sigma u} = 1.98$) to $\tilde{x} = 6$, with a maximum thickness exceeding 10% of the throat height. The maximum reversed velocity occurs at $\tilde{x} = 3.46$ and equals $\approx 25\%$ of the local core flow speed.

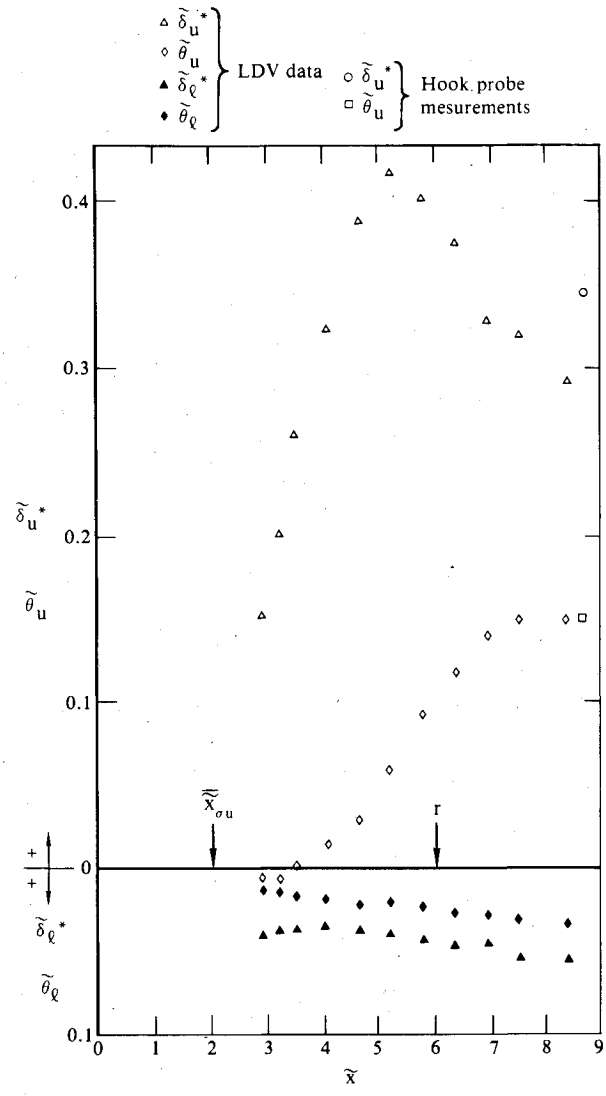

Fig. 9 Boundary-layer thickness distribution for strong shock case ($M_{\sigma u} = 1.353$). Arrows labeled $\tilde{x}_{\sigma u}$ and r indicate mean positions of shock and reattachment of separation bubble on top wall.

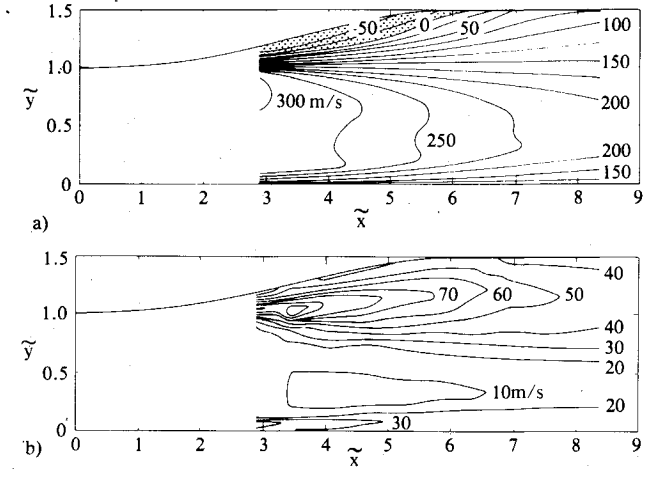

Fig. 10 Velocity contours of unexcited flow, $M_{\sigma u} = 1.353$; a) mean velocity $\bar{u}$ (shaded areas denote reverse flow), b) fluctuating velocity $\hat{u}$.

The rms values of the fluctuating velocity component (Fig. 10b) reflect the asymmetry found in terms of mean velocities. Top-wall fluctuation levels are nearly triple the weak shock values and peak along the line where the vertical gradient of the mean streamwise velocity is maximum. The top-wall

intensity reaches a maximum near the midpoint of the separation bubble ($\tilde{x}=3.5$), well upstream of the location where the displacement thickness is the greatest ($\tilde{x}=5.5$). The bottom-wall fluctuations are approximately at the weak shock level and confined to an even thinner layer.

Strong Shock—Excitation at 300 Hz

The ensemble-averaging procedure described earlier resulted in a velocity waveform for each point of the spatial matrix. The mean values computed from such waveforms were assembled into the contour plot of Fig. 11a, which is similar to the mean flowfield obtained without excitation (Fig. 10a). The velocity profiles near reattachment are not as fully developed in the excited case, but otherwise the mean flow is unaffected by the imposition of the perturbations.

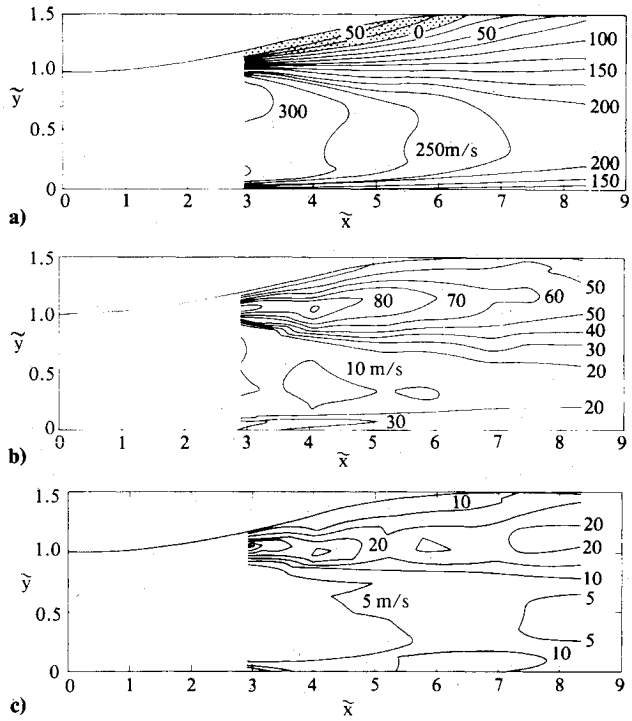

Fig. 11 Velocity contours of excited flows, $M_{au}=1.353$ and $f=300$ Hz; a) mean velocity $\bar{u}$ (shaded areas denote reverse flow), b) random fluctuating velocity $\hat{u}$, c) rms streamwise periodic velocity u.

Random contributions to the velocity fluctuations, $\hat{u}$, are given in Fig. 11b. Comparison with the unexcited case (Fig. 10b) reveals nearly identical levels throughout the flowfield. Significant differences exist only on the top wall, near and downstream of reattachment where the excited flow shows about 10-20% greater random fluctuation intensities. The peak intensity in the top layer is more than twice as large as the peak within the bottom layer.

The comparison of the mean and random fluctuating velocity fields thus indicates that the original turbulent flowfield is altered only mildly by the superimposed perturbations. The periodic contribution to the flowfield apparently coexists with the naturally present fluctuation field without being coupled to it significantly.

As is evident from Figs. 11b and 11c, the rms intensities of the periodic field are considerably below those of the random contributions; the signal-to-noise ratio of the original signal is approximately 0.3, and ensemble averaging over a large number of cycles is essential for accurate determination of the waveforms. In contrast to the unexcited case, the spatial distribution of the amplitudes of the periodic field is not monotonic with $\tilde{x}$. There is a local maximum in the core flow near $\tilde{x}=6.5$ with several local minima; one in the core toward the throat and one at about the same height at the extreme downstream position. Most of the fluctuations are within the boundary layers, which is at variance with the expectation of a more-or-less one-dimensional pattern caused by acoustic waves propagating in both directions.

The time dependence of these fluctuations is illustrated by a series of contour plots for u (the instantaneous perturbation velocity) at six equal increments of the perturbation phase α (Fig. 12). The plots are reconstructions, using the first five Fourier harmonics of the original data set. Shaded areas indicate negative u values, i.e., regions where the instantaneous velocity is below the local mean velocity. The plots also indicate the instantaneous location of the shock obtained by an independent optical technique. The sequence

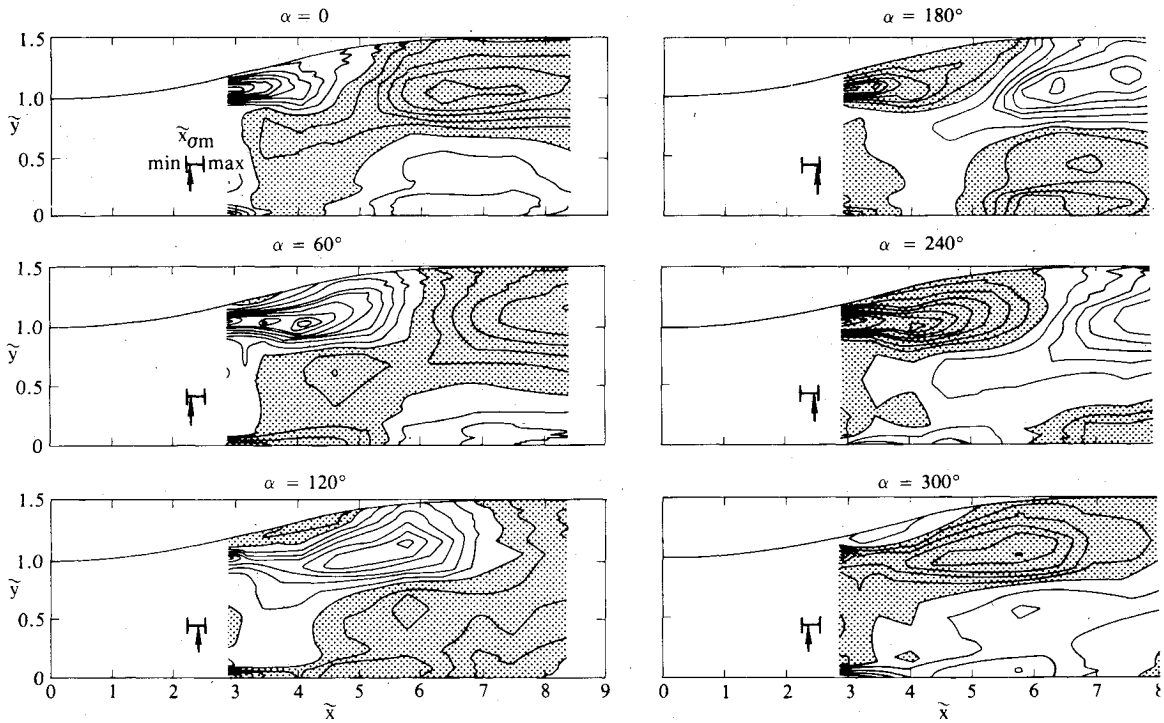

Fig. 12 Temporal development of streamwise perturbation flow over one period of oscillation, $M_{au}=1.353$ and $f=300$ Hz.

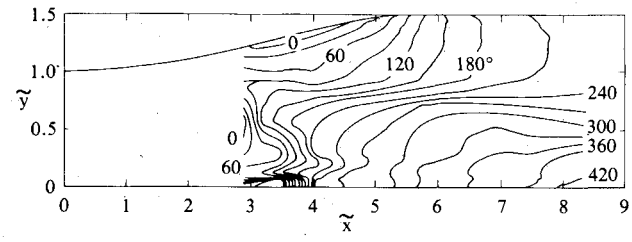

Fig. 13 First harmonic phase ϕ_1 of the periodic velocity component, $M_{ou} = 1.353$ and $f = 300$ Hz.

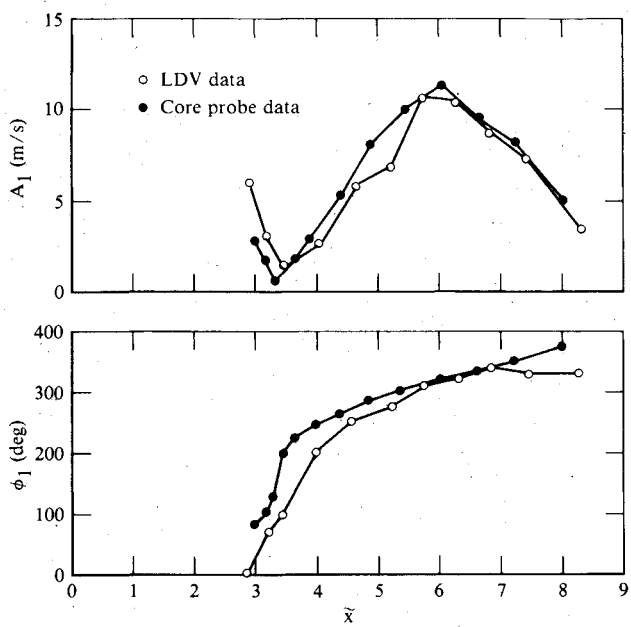

Fig. 14 First harmonic amplitude and phase of streamwise perturbation flow, $M_{ou} = 1.353$, $f = 300$ Hz, and $\tilde{y} = 0.432$.

shows clearly defined, large zones of coherent perturbations, moving in the downstream direction at a somewhat uneven, approximate speed of one-half of the local core flow speed. Perturbations at the top and bottom are out of phase by approximately 180 deg, indicating a transverse "flapping" of the instantaneous flow pattern. This transverse motion together with the strong velocity gradients present in the boundary layer are responsible for the fact that periodic fluctuations are concentrated in the boundary layer.

The transverse motion is originated by the shock, whose periodically varying position and strength imprints a corresponding modulation on the boundary layer emerging from the shock/boundary-layer interaction. The waves then move downstream at the speed indicated by the movement of the correlated regions in Fig. 12. The shock also modulates the separation bubble embedded in the boundary layer, the primary effect being a pulsation of the bubble thickness.

Some features of the perturbation flowfield can be highlighted more clearly by examining the first Fourier component only. The phase angle of the first harmonic ϕ_1, referenced to the instant of maximum blockage by the exciter, is illustrated in Fig. 13. This representation is appropriate to indicate directions in which the resultant perturbations propagate because the direction is everywhere normal to the constant phase-angle lines and directed toward increasing ϕ. The plot indicates that the disturbance originates along the top wall inside the separation bubble and propagates downstream within the upper-wall boundary layer. In the core this propagation becomes transverse to the mean flow and continues downstream as it approaches the bottom wall.

Figure 14 illustrates the streamwise distributions of the amplitude and phase of the first harmonic for a horizontal line lying in the core flow at $\tilde{y} = 0.432$, as obtained with the LDV system and also with an independent technique using high-response pressure transducers.[2] Considering the difficulties associated with either technique, agreement is good. The amplitude distributions define a perturbation velocity node at $\tilde{x} = 3.4$ and strongly suggest another at $\tilde{x} \cong 9$, whichis a location outside the range of both measurements. The abrupt 180 deg phase shift characterizing a nodal line in the core flow is smeared over a streamwise distance of roughly one throat height, but is otherwise clearly recognizable. The gradual phase shift beyond $\tilde{x} = 3.8$ is another manifestation of the downstream movement of the periodic perturbations already discussed.

Concluding Remarks

Data obtained for the weak shock case describe a reasonably well-behaved, nearly two-dimensional velocity field. The flowfield is amenable to theoretical modeling as a combination of an inviscid freestream and two properly matched boundary layers, as demonstrated in Ref. 8.

The unsteady perturbation velocity field in the strong shock case is more complex. The excited flow displays a strong asymmetry and significant vertical gradients (Figs. 11-13), which appear to be governed by the original, similarly asymmetric unperturbed flow (Fig. 10). However, the possibility should not be dismissed that the method of excitation (applied on one wall only) may be responsible in part for some of the asymmetry and/or the transverse variations.

Apart from the random fluctuation intensities $\hat{u}$ (Figs. 10b and 11b), the measurements yield no information on the naturally present fluctuations. These fluctuations are known to be coherent over most of the diffuser,[1] but the spatial details are not well known, and the natural field could, in principle, be qualitatively different from the measured perturbation field. The lack of coupling between the forced and natural flowfields is compatible with this possibility. Since the natural fluctuations are only approximately periodic (the spectral peak is moderately broad), determination of the associated spatial distributions would be difficult. Fortunately, the extent of such possible dissimilarities has little effect on the utility of the presented data for verifying relevant theoretical computation methods.

An accurate prediction of the strong shock case demands a comprehensive theory that properly includes the strong viscous-inviscid interactions characterizing the flow. Computations based on the mass-averaged Navier-Stokes equations, the Wilcox-Rubesin two-equation turbulence model, and MacCormack's time-dependent algorithm achieved considerable success in duplicating details of the mean flow.[9,10]

The types of flows investigated here are often described for engineering purposes, such as in ramjet design, by inviscid, unsteady, one-dimensional, linearized (acoustic) calculations.[3,11] The results of Ref. 1 suggest that this simple approximation, when used in conjunction with appropriate reflection conditions at the shock,[12] produces a reasonable description of the natural oscillatory flowfield and predicts the correct natural frequencies for the weak shock case. However, the description fails in the case of strong shocks involving shock-induced separation. The roots of the discrepancy lie in the neglect of the major role played by the boundary layers, which are induced to grow at high rates by the shock/boundary-layer interaction. Most of the fluctuations occur in the boundary layers (not in the inviscid core), the fluctuations are transverse (not longitudinal), and the velocity fluctuation magnitudes are far above what acoustic theory predicts for the measured pressure fluctuations. Acoustic waves propagating in both directions are undoubtedly present but are overwhelmed by the transverse waves of the boundary-layer/core flow interface that are convective and strongly influenced by viscous-inviscid interactions.

Acknowledgment

This work was sponsored by the McDonnell Douglas Corporation Independent Research and Development Program.

References

[1]Bogar, T. J., Sajben, M., and Kroutil, J. C., "Characteristic Frequencies of Transonic Diffuser Flow Oscillations," *AIAA Journal*, Vol. 21, Sept. 1983, pp. 1232-1240.

[2]Sajben, M., Bogar, T. J., and Kroutil, J. C., "Forced Oscillation Experiments in Supercritical Diffuser Flows with Application to Ramjet Instabilities," AIAA Paper 81-1487, 1981, *AIAA Journal*, to be published.

[3]Rogers, T., "Ramjet Inlet/Combustion Pulsations Study," Naval Weapons Center, China Lake, CA, Rept. NWC TP 6053, Jan. 1980.

[4]Sajben, M., Kroutil, J. C., and Chen, C. P., "A High-Speed Schlieren Investigation of Diffuser Flows with Dynamic Distortion," AIAA Paper 77-875, 1977.

[5]Sajben, M., Kroutil, J. C., and Chen, C. P., "Unsteady Transonic Flow in a Two-Dimensional Diffuser," AGARD CP 227, Unsteady Aerodynamics, 1977, pp. 13-1 to 13-14.

[6]Chen, C. P., Sajben, M., and Kroutil, J. C., "Shock-Wave Oscillations in a Transonic Diffuser Flow," *AIAA Journal*, Vol. 17, Oct. 1979, pp. 1076-1083.

[7]Sajben, M. and Kroutil, J. C., "Effects of Initial Boundary-Layer Thickness on Transonic Diffuser Flows," *AIAA Journal*, Vol. 19, Nov. 1981, pp. 1386-1393.

[8]Liou, M. S., "Analysis of Viscous-Inviscid Interaction in Transonic Internal Flows," *AIAA Journal*, Vol. 21, July 1983, pp. 962-969.

[9]Coakley, T. J. and Bergmann, M. Y., "Effects of Turbulence Model Selection on the Prediction of Complex Aerodynamic Flows," AIAA Paper 79-0070, 1979.

[10]Liou, M. S., Coakley, T. J., and Bergmann, M. Y., "Computations of Transonic Diffuser Flows," NASA Lewis Research Center, Proceedings of Workshop on Advanced Computational Methods for Inlets, Diffusers, and Nozzles, Nov. 1980.

[11]Culick, F. E. C. and Rogers, T., "Modeling Pressure Oscillations in Ramjets," AIAA Paper 80-1192, 1980.

[12]Culick, F. E. C., "The Response of Normal Shocks in Inlet Diffusers," AIAA Paper 81-1431, 1981.